Anal. Chem. **2007,** *79,* 3048−3055

Fabrication of Nanopore Array Electrodes by Focused Ion Beam Milling

Yvonne H. Lanyon,† Gianluca De Marzi,† Yvonne E. Watson,† Aidan J. Quinn,† James P. Gleeson,‡ Gareth Redmond,† and Damien W. M. Arrigan*,†

Tyndall National Institute, Lee Maltings, and Department of Applied Mathematics, University College, Cork, Ireland

Single nanopore electrodes and nanopore electrode arrays have been fabricated using a focused ion beam (FIB) method. High aspect ratio pores (∼150−400-nm diameter and 500-nm depth) were fabricated using direct-write local ion milling of a silicon nitride layer over a buried platinum electrode. This local milling results in formation of a recessed platinum electrode at the base of each nanopore. The electrochemical properties of these nanopore metal electrodes have been characterized by voltammetry. Steady-state voltammograms were obtained for a range of array sizes as well as for single nanopore electrodes. High-resolution scanning electron microscopy imaging of the arrays showed that the pores had truncated cone, rather than cylindrical, conformations. A mathematical model describing diffusion to an electrode located at the base of a truncated conical pore was developed and applied to the analysis of the electrode geometries. The results imply that diffusion to the pore mouth is the dominant mass transport process rather than diffusion to the electrode surface at the base of the truncated cone. FIB milling thus represents a simple and convenient method for fabrication of prototype nanopore electrode arrays, with scope for applications in sensing and fundamental electrochemical studies.

The development of ultrasmall electrodes offers numerous advantages to electrochemistry and analytical chemistry.[1−4] First, mass transport rates to very small electrodes are greater than at regularly sized (i.e., millimeter) electrodes, offering scope for kinetic measurements of faster chemical processes. This enhanced mass transport, which comes from the predominance of three-dimensional diffusion to such small electrodes, also offers improvements for analytical and sensor applications in terms of a shorter response time and increased sensitivity. These applications have been the subject of numerous investigations at micrometer-sized electrodes and their arrays.[1−4] Second, smaller electrode size enables a higher density of transducers to be fabricated on each sensor device, such as a sensor chip, thus yielding a higher information-generating capability per device. Attempts to work at smaller (i.e., submicrometer) electrode sizes have been the subject of fewer reports, reflecting the difficulties in the preparation of nanometer-sized electrodes.[5−8] However, the goal of sensor applications such as single-molecule detection and achieving the ultimate in device miniaturization remains an important driving force in this area.

The most popular fabrication methods for nanoelectrodes are the preparation of single electrodes by coating of electrochemically etched microelectrodes with electrophoretic paint[7,9−13] or by stretching of metal wires sealed in glass.[8,14] Nanoelectrode ensembles have also been prepared by deposition of metal into the pores of nanoporous filtration membranes.[6,15] With these methods, single nanoelectrodes with radii from 2 nm up to 1000 nm have been fabricated. Steady-state voltammetric curves can be obtained at single nanoelectrodes, but the ensembles produced by the membrane deposition procedure result in the overlap of diffusion layers at individual electrodes, leading to non-steady-state responses. Sensor and related analytical applications of these types of electrodes are of interest, but widespread take-up is limited by the manual preparation procedures. Recent advances in nanoelectrode fabrication include a chemical (solvent) etch of polymer membranes containing embedded nanowire arrays[16] and electron beam lithography for preparation of single nanoelectrodes.[17] Low-density carbon nanotube arrays, which possess sufficient intertube spacings to prevent overlap of diffusion layers at adjacent nanotubes, have also emerged as approaches to sensor applications of nanoelectrodes.[18−20]

* To whom correspondence should be addressed. E-mail: damien.arrigan@tyndall.ie. Fax: +353-21-4270271. Phone: +353-21-4904079.

† Tyndall National Institute.

‡ Department of Applied Mathematics.

(1) Forster, R. J. *Chem. Soc. Rev.* **1994**, *23*, 289−297.
(2) Zoski, C. G. *Electroanalysis* **2002**, *14*, 1041−1051.
(3) Bond, A. M. *Analyst* **1994**, *119*, R1−R21.
(4) Wightman, R. M.; Wipf, D. O. In *Electroanalytical Chemistry*; Bard, A. J., Ed.; Marcel Dekker: New York, 1989; Vol. 15, p 267.
(5) Arrigan, D. W. M. *Analyst* **2004**, *129*, 1157−1165.
(6) Ugo, P.; Moretto, L. M.; Vezza, F. *ChemPhysChem* **2002**, *3*, 917−925.
(7) Slevin, C. J.; Gray, N. J.; Macpherson, J. V.; Webb, M. A.; Unwin, P. R. *Electrochem. Commun.* **1999**, *1*, 282−288.
(8) Ballesteros Katemann, B.; Schuhmann, W. *Electroanalysis* **2002**, *14*, 22−28.
(9) Watkins, J. J.; White, H. S. *Langmuir* **2004**, *20*, 5474−5483.
(10) Watkins, J. J.; Chen, J. Y.; White, H. S.; Abruna, H. D.; Maisonhaute, E.; Amatore, C. *Anal. Chem.* **2003**, *75*, 3962−3971.
(11) Conyers, J. L., White, H. S. *Anal. Chem.* **2000**, *72*, 4441−4446.
(12) Chen, S.; Kucernak, A. *Electrochem. Commun.* **2002**, *4*, 80−85.
(13) Chen, S.; Kucernak, A. *J. Phys. Chem.* **2002**, *106*, 9396−9404.
(14) Shao, Y.; Mirkin, M. V.; Fish, G.; Kokotov, S.; Palanker, D.; Lewis, A. *Anal. Chem.* **1997**, *69*, 1627−1634.
(15) Kohli, P.; Wirtz, M.; Martin, C. R. *Electroanalysis* **2004**, *16*, 9−18.
(16) Krishnamoorthy, K.; Zoski, C. G. *Anal. Chem.* **2005**, *77*, 5068−5071.
(17) Lemay, S. G.; van den Broek, D. M.; Storm, A. J.; Krapf, D.; Smeets, R. M. M.; Heering, H. A.; Dekker, C. *Anal. Chem.* **2005**, *77*, 1911−1915.
(18) Li, J.; Koehne, J. E.; Cassell, A. M.; Chen, H.; Ng, H. T.; Ye, Q.; Fan, W.; Han, J.; Meyyappan, M. *Electroanalysis* **2005**, *17*, 15−27.

10.1021/ac061878x CCC: $37.00
Published on Web 03/20/2007

Preparation of microelectrode arrays using photolithographic microfabrication methods is in wide use.[21,22] Typically in these systems, the area of the metal electrodes is defined by opening up micrometer-sized apertures in passivation layers placed on top of the electrode metal. Here we report on application of this approach to the fabrication of nanoelectrodes and nanoelectrode arrays. In essence, a metal layer on a suitable substrate is covered with a passivation layer, e.g., silicon nitride, and pores in that layer are opened by a method suited to nanoscale pore formation. Focused ion beam (FIB)[23] milling is one such method. The pores allow access of electrolyte to the underlying metal electrode surface when the device is immersed into an electrolyte solution and allows electrochemical characterization. The benefits of using FIB in this manner is that it is a direct-write method and aids the rapid prototyping of electrodes and arrays, in contrast to electron beam lithography,[24] which requires more processing steps. On the other hand, FIB milling is a serial method, with each electrode in an array being prepared individually. Although FIB milling has been recently reported for preparation of single tungsten electrodes for neurophysiology,[25] by milling through electrophoretically deposited paint, we are not aware of its use in preparation of arrays of devices. Here we report on the fabrication of experimental prototypes of nanopore array electrodes and their electrochemical characterization. Based on observations, it was apparent that the pores were not cylindrical but had a truncated cone shape. An analytical model for the current at a disk electrode located at the base of a truncated conical pore is also presented and used for characterization of the nanopore electrodes.

EXPERIMENTAL SECTION

Fabrication. Nanopore array electrodes were fabricated on oxidized silicon wafer substrates. Platinum electrodes (100 nm thick) were fabricated using UV lithography, metal deposition, and liftoff. The electrodes used had dimensions of 1.5 mm × 1 mm. A silicon nitride film (500 nm thick) was then deposited to form an insulating layer over the buried electrodes. Bond pads for formation of electrical contacts to the buried metal electrodes were opened using UV lithography and etching. Each wafer was then diced into individual die, with each die containing four buried electrode devices and electrical contact pads. A FIB system (FEI Vectra 200DE, 30-keV Ga ions, 10-nm nominal spot diameter, 10-pA beam current) was employed for direct-write nanoscale milling of the silicon nitride passivation layer. Single nanopores and nanopore arrays with controlled-pore diameters and pore−pore spacings were fabricated using sequential milling. On each die, one device was employed as a control sample to determine the milling time required to reveal the buried platinum electrode at the base of the pore. An end point detection method was employed, whereby the ion beam current measured at the sample

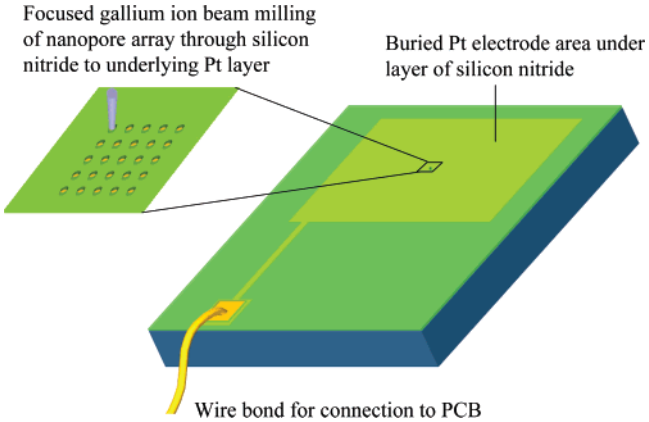

Figure 1. General schematic of the fabrication strategy. Pt surface covered with silicon nitride is milled by focused ion beam to open up nanopores through to the underlying Pt.

substrate was recorded as a function of the milling time. A sharp increase in current is observed as the beam reaches the platinum layer, at which point the process can be stopped. This milling time (~40 s) was then employed for each pore fabricated on the remaining three devices on the die. Following fabrication of the individual nanopores or nanopore arrays, each chip was mounted on a plastic printed circuit board, electrically contacted using wire bonding, and packaged using epoxy resin to seal the electrical connections and the chip edges.

Characterization. The nanopore electrodes (and their arrays) were structurally characterized using a field emission scanning electron microscope (6700F SEM, Jeol Ltd.) operating at beam voltages between 3 and 10 kV. All electrochemical measurements were performed with CH Instruments potentiostats, either CH620 or CH660, using a three-electrode electrochemical cell. Characterization of the nanopore electrodes was undertaken using cyclic voltammetery (CV) in the potential range 0.0 to +0.6 V. Square wave voltammetry was conducted over the same potential window with an increment potential of 4 mV, a pulse amplitude of 25 mV, and a frequency of 5 Hz. An aqueous solution of ferrocenemonocarboxylic acid (FcCOOH) at 1 mM in 0.01 M phosphate-buffered saline (PBS) pH 7.4 was used as the test electrolyte solution. The working electrodes were the platinum nanopore electrodes (or arrays) under investigation, the reference electrode was Ag|AgCl|KCl(3 M), and the counter electrode was a platinum wire. All nanopore electrodes were cleaned with oxygen plasma (150 W, 10 min) and rinsed with deionized water prior to use.

RESULTS AND DISCUSSION

Fabrication and SEM Characterization. Figure 1 illustrates the principle of the FIB milling approach used, producing nanopore-recessed electrodes and arrays. This is a simple and rapid technique, where the direct-write approach and ability to process small numbers of samples at a time (rather than whole wafers) allows rapid formation of prototype nanopore electrodes. Each individual silicon die consisted of four buried working electrode areas (each separately connected), over which nanopore formation in the insulating silicon nitride was achieved using the FIB milling approach. This involves the spatially resolved ion milling of the silicon nitride thin layer (500-nm thickness) with a finely focused beam of gallium ions targeted at the surface. The

(19) Tu, Y.; Lin, Y. H.; Yantasee, W.; Ren, Z. F. *Electroanalysis* **2005**, *17*, 79−84.
(20) Liu, G. D.; Lin, Y. H.; Tu, Y.; Ren, Z. F. *Analyst* **2005**, *130*, 1098−1101.
(21) Le Drogoff, B.; El Khakani, M. A.; Silva, P. R. M.; Chaker, M.; Vijh, A. K. *Electroanalysis* **2001**, *13*, 1491−1496.
(22) Berduque, A.; Lanyon, Y. H.; Beni, V.; Herzog, G.; Watson, Y. E.; Rodgers, K.; Stam, F.; Alderman, J.; Arrigan, D. W. M. *Talanta* **2007**, *71*, 1022−1030.
(23) Langford, R. M. *J. Nanosci. Nanotechnol*. **2006**, *6*, 661−668.
(24) Sandison, M. E.; Cooper, J. M. *Lab Chip* **2006**, *6*, 1020−1025.
(25) Qiao, Y.; Chen, J.; Guo, X.; Cantrell, D.; Ruoff, R.; Troy, J. *Nanotechnology* **2005**, *16*, 1598−1602.

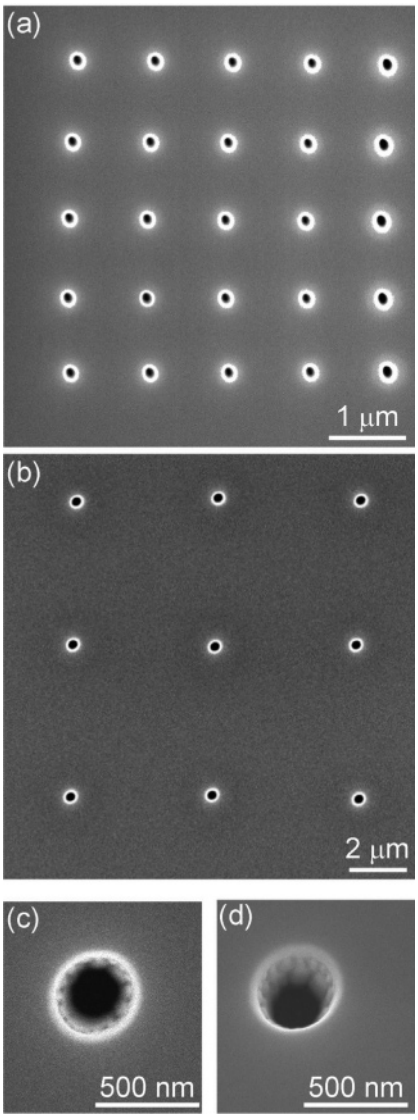

Figure 2. SEM images of nanopore electrode arrays and single nanopore electrodes: (a) 5 × 5 array; (b) 3 × 3 array; (c) single nanpore; and (d) 10° tilted image of single nanopore shown in (c).

milling rate varies with the ion beam current used, so in this work, a relatively small beam current, 10 pA, was used for the milling of pores with nanoscale dimensions. Nanopores with diameters in the range 150−400 nm were fabricated, with varying numbers per array, from single pores to arrays of 225 pores. The 150-nm-diameter pores were close to the lower limits of pore diameters that could be achieved for these devices, due to the high aspect ratios of the pores and the beam diameter. Fabrication of arrays was possible by using the FIB to drill at chosen locations across the silicon nitride surface. Large pore−pore distances were selected in this work, in order to avoid overlap of diffusion fields at closely spaced pores during subsequent electrochemical studies. Figure 2 shows the SEM images from a selection of arrays and single electrodes with varying diameters.

From Figure 2, it can be seen that disk-shaped pores were opened up in the silicon nitride layer and that arrays of varying size can be produced by sequential milling of pores. It is also apparent, on close examination of the single nanopores, that the mouth of the pore is wider than the visible base. This gives the impression of a truncated cone shape. However, it should be noted

Table 1. Parameters for Nanopore Electrodes Derived from Analytical Models for Steady-State Currents at Electrodes[a]

array	r_L (SEM)/ nm	r (eq 2)[b]/ nm	r_0 (eq 3)[c] nm	wall angle/ deg
15 × 15	225	212	197	3.2
5 × 5	75	73	70	0.3
5 × 5	100	62	37	7.2
3 × 3	225	216	204	2.4
1	225	211	195	3.4

[a] L = 500 nm in all cases. For r_0 (eq 3), r_L = the SEM value. Wall angle = $\tan^{-1}[(r_L - r_0)/L]$. [b] Cylinder-recessed disk electrode. [c] Truncated cone-recessed disk electrodes.

that the apparent thickness of the silicon nitride layer obtained from the angled SEM images is thinner than the actual fabricated thickness. Therefore, we assume that the bottom of the pore is not visible by SEM (Figure 2). Topview images of nanopores enabled viewing of the inner walls right around the pore (Figure 2c). Upon tilting a nanopore sample by 10°, the lower part of the wall was no longer visible, suggesting that the wall angle of these cones was 10° or less. The formation of conical pores by FIB milling has been reported[23,26] to be caused by redeposition of milled material; wall angles of 2−10° have been obtained previously. Our wall angles of ≤10° are consistent with this range. We note that Santschi et al.[27] have recently employed XeF_2 enhanced FIB milling in order to reduce the effects of material redeposition in the fabrication of interdigitated nanogap nanoelectrodes.

Table 1 summarizes the radii of the mouths of the pores obtained from SEM images. We refer to the radius at the mouth of the cone as r_L, where L is the thickness of the passivation layer of silicon nitride. For some of the arrays prepared, it can be seen that the pore mouth radius, r_L, at 225 nm, means that the pore mouth diameter is equivalent to the thickness of the silicon nitride passivation layer, $2r/L$ is ∼1. The reproducibility of the pore diameters obtained by FIB milling is summarized in Table 2a from which an overall (i.e., all data at all array electrodes) relative standard deviation (RSD) of 6% was obtained, based on a total of 16 SEM measurements of four separate arrays. Intra-array pore diameter reproducibility ranged from 3 to 5% RSD (Table 2a). The radius at the base of the cone, r_0, was not determinable by SEM directly, because the base of the pore was not visible, as discussed above, or by cross-sectional cutting of the pores. Nevertheless, the location of the electrode surface at the base of such a truncated cone has implications for the diffusion of electroactive species to these electrodes during electrochemical experiments and, hence, for the current and interpretation of the current as a function of the electrode dimensions.

Voltammetry at Nanopore Array Electrodes. Figure 3a shows typical CVs for FcCOOH in PBS, pH 7.4, for the arrays prepared in this study. It is obvious from this figure that (i) the arrays produce a steady-state voltammetric response, signifying that diffusion to the electrodes is rapid, and is independent to each pore in the array; and (ii) the steady-state current scales

(26) Wei, H. X.; Langford, R. M.; Han, X.; Coey, J. M. D. *J. Appl. Phys.* **2006**, *99*, 08C501.
(27) Santschi, C.; Jenke, M.; Hoffmann, P.; Brugger, J. *Nanotechnology* **2006**, *17*, 2722−2729.

Table 2

(a) Reproducibility of FIB Nanopore Diameters

array	nanopore ø mean[a]/nm	SD[b]/nm	RSD/%
5 × 5 a	162	4	3
5 × 5 b	148	5	3
5 × 5 c	162	8	5
5 × 5 d	166	6	4

(b) Reproducibility of Voltammetric Measurements

array	current mean[c]/pA	SD[d]/pA	RSD/%
3 × 3 a	125	23.3	19
3 × 3 b	147	21.1	14
3 × 3 c	123	13.8	11
5 × 5 a	26	1.62	6
5 × 5 b	30	0.27	1
5 × 5 c	14	2.06	15

[a] Data based on four separate SEM pore measurements for each array, taken from inner halo diameter around pore mouth. [b] SD, standard deviation, $n = 4$. [c] Data based on the steady-state current from triplicate CV measurements using (i) 3 × 3 arrays with 225-nm pore radii and (ii) 5 × 5 arrays with 80-nm pore radii. [d] SD, standard deviation, $n = 3$.

with the number of nanopores per array, for pores of equal dimensions. An increase in the CV scan rate from 5 to 100 mV s^{-1} did not cause an increase in the faradic current or change in the wave shape (Figure 3b), as expected from inlaid disk microelectrodes with sufficient interelectrode spacing. This prevalence of radial diffusion at higher scan rates implies that the response is controlled by diffusion to the pore mouth rather than to the disk electrode at the base of the pore. An increase in the capacitance current was noted at higher scan rates, indicated by the increased separation between the forward and reverse CV scans as shown in Figure 3b. Capacitance currents are discussed below. The reproducibility of the CV measurements is summarized in Table 2b based on data from 3 × 3 arrays with 225-nm pore radii and 5 × 5 arrays with 80-nm pore radii. The overall (i.e., all measurements at all arrays of each type) reproducibilities were 16 and 32% RSD for the 3 × 3 and 5 × 5 arrays, respectively (based on triplicate CV measurements of three separate arrays in each case). Intra-array reproducibility was in the range 11−19% RSD for the 3 × 3 arrays and 1−15% RSD for the 5 × 5 arrays (based on triplicate CV measurements). The interarray RSD of the voltammetric data (Table 2b) is higher than that obtained from the outer diameter pore measurements. This may be attributed to remnant silicon nitride debris at the bottom of the pores following FIB milling, causing partial insulation of the electrode surface (some pores perhaps with more debris than others).

Use of electrochemistry together with imaging to monitor and characterize electrodes of very small dimensions is a common approach.[7−13] For example, the nanoscale electrodes created by etching of conductor and sealing of the etched tip with a passivating material (e.g., electrophoretic paint,[7,9−13] silicon rubber[28]) are characterized by assuming the electrodes behave as inlaid disks, in which case the limiting current value is described by the Saito equation (eq 1),[29]

$$I_{\mathrm{lim}} = 4nFDC^{\mathrm{b}}\mathrm{r} \qquad (1)$$

where I_{lim} is the limiting or steady-state current, n is the number of electrons transferred per molecule in the electrochemical reaction, F is the Faraday constant, D the diffusion coefficient, C^{b} the bulk solution concentration of the redox-active species, and r the radius of the disk electrode. Clearly, for the work detailed here, where the pore mouth diameter to pore depth ratio is close to 1, the Saito model (eq 1) will be insufficient for characterization of the pores as it does not account for location of the electrode at the base of a well. Additionally, remnants of debris from the FIB milling of the silicon nitride may occupy part of the electrode surface area, thus resulting in a lower apparent radius.

A model for the steady-state limiting current at a recessed electrode was presented by Bond et al.[30] This model (eq 2) shows the dependence of the limiting current at a recessed disk microelectrode as a function of both the disk radius and the recess depth, L.

$$I_{\mathrm{lim}} = \frac{4\pi nFC^{\mathrm{b}}Dr^2}{4L + \pi r} \qquad (2)$$

(all parameters have their previous meanings). This model has been used in the estimation of recessed nanoelectrode parameters.[31−33] Application of eq 2 to the estimation of the apparent radii of the nanopore electrodes of this work is shown in Table 1 (the column headed by r(eq 2)). Evidently, the apparent electrode radii are smaller than the pore mouth radii obtained from the SEM images, but nevertheless in close agreement. This level of agreement between the pore mouth radii (r_{l}) determined by SEM images and by application of eq 2 may be because the recess wall angle, at ≤10°, is close enough to the vertical to enable application of this model.

The Bond et al.[30] model (eq 2), however, assumes a vertical recess wall so that diffusion to the electrode at the bottom of the pore is as through a cylinder and is one-dimensional. Figure 4 summarizes the diffusion fields present for the above models at steady state and the intuitive difference between those and the present recessed nanopore array electrodes is obvious. It is apparent, in terms of hindrance of diffusion to the electrode surface, that the electrodes located at the base of truncated nanocones are intermediate between the inlaid disk and the case of a disk recessed at the base of a cylinder. Thus, a disk recessed within a truncated cone should conceptually have a less-hindered diffusion profile than that recessed within a cylinder. Given the similarities between the SEM data and the data derived from combination of electrochemical measurements with the recessed disk model (eq 2), it may well be that the controlling mass transport is diffusion to the pore opening (mouth of truncated

(28) Hrapovic, S.; Luong, J. H. T. *Anal. Chem.* **2003**, *75*, 3308−3315.
(29) Saito, Y. *Rev. Polarogr. Jpn.* **1968**, *15*, 177.
(30) Bond, A. M.; Luscombe, D.; Oldham, K. B.; Zoski, C. G. *J. Electroanal. Chem.* **1988**, *249*, 1−14.
(31) Fan, F.-R. F.; Kwak, J.; Bard, A. J. *J. Am. Chem. Soc.* **1996**, *118*, 9669−9675.
(32) Kralj, B.; Dryfe, R. A. W. *Phys. Chem. Chem. Phys.* **2001**, *3*, 3156−3164.
(33) Henry, C. S.; Fritsch, I. *Anal. Chem.* **1999**, *71*, 550−556.

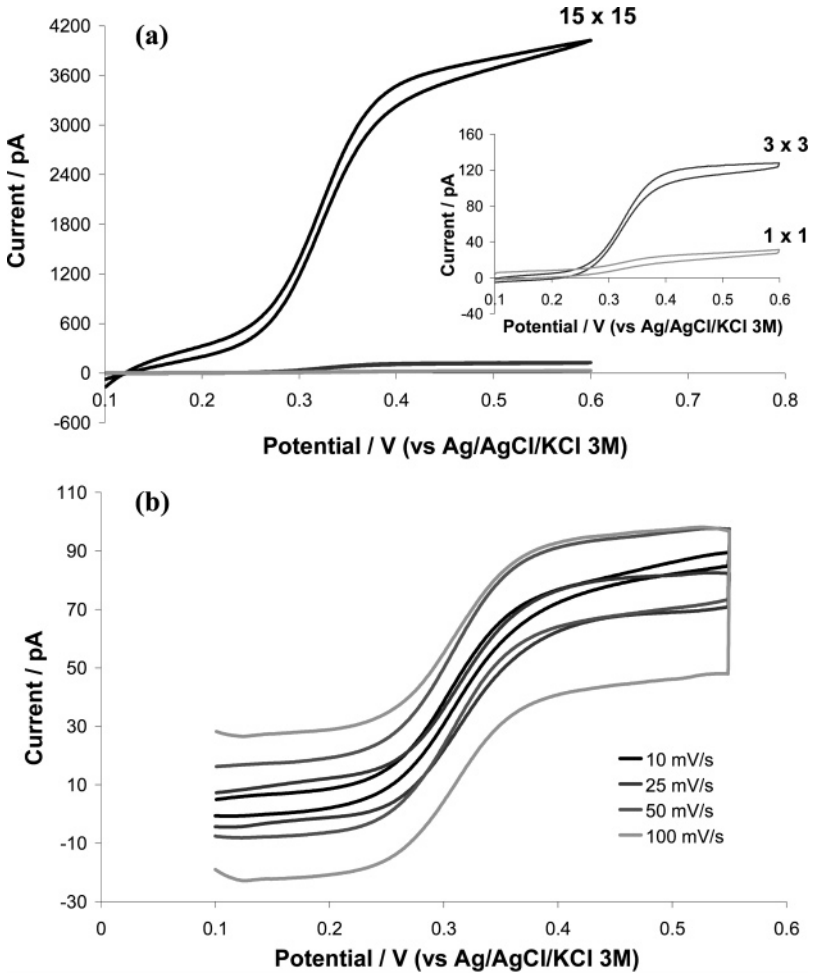

Figure 3. Voltammetric characterization of selected nanopore electrode arrays using 1 mM FcCOOH in PBS. (a) The influence of increasing nanoelectrode numbers on the CV response at 5 mV s^{-1} based on arrays with pore radii of 225 nm; (b) the influence of increasing CV scan rates on a 3 × 3 nanopore array with pore radii of 80 nm and a ratio of interpore spacing to pore radius of 63.

pore) rather than to the pore base. Such a scenario is then directly opposite to the lagoon electrodes described by Oldham[34] and Baranski[35] and the nanopore electrode of White and co-workers,[36–38] where the pore opening is smaller than the disk electrode at the base of the pore. Given the apparent location of the electrodes in this work at the base of a truncated cone, an expression for the diffusion-controlled steady-state current at such electrodes was developed.

Diffusion-Controlled Current at a Disk Located at the Base of a Truncated Cone. Figure A1 (Supporting Information) summarizes the truncated cone geometry modeled. Full details of the derivation are given in the Supporting Information. The disk electrode is located at the base ($z = 0$) with radius r_0. The mouth of the cone has radius r_L, with $r_L > r_0$. The steady-state limiting current can be written in terms of the radii (eq 3) or the wall angle α (eq 4):

$$I_{lim} = \frac{4\pi nFC^b D r_0 r_L}{4L + \pi r_0} \quad (3)$$

$$I_{lim} = \frac{4\pi nFC^b D r_L (r_L - L\tan\alpha)}{4L + \pi(r_L - L\tan\alpha)} \quad (4)$$

Comparison of the currents for eqs 1 and 2 with the truncated

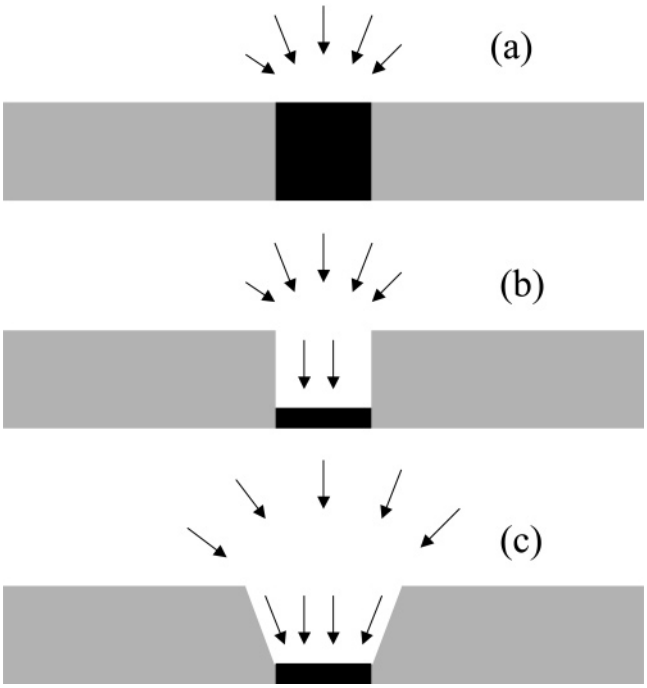

Figure 4. Sketches of diffusion profiles to (a) inlaid, (b) recessed (cylinder), and (c) recessed (truncated cone) electrodes. The arrows represent the diffusion profiles to the electrodes.

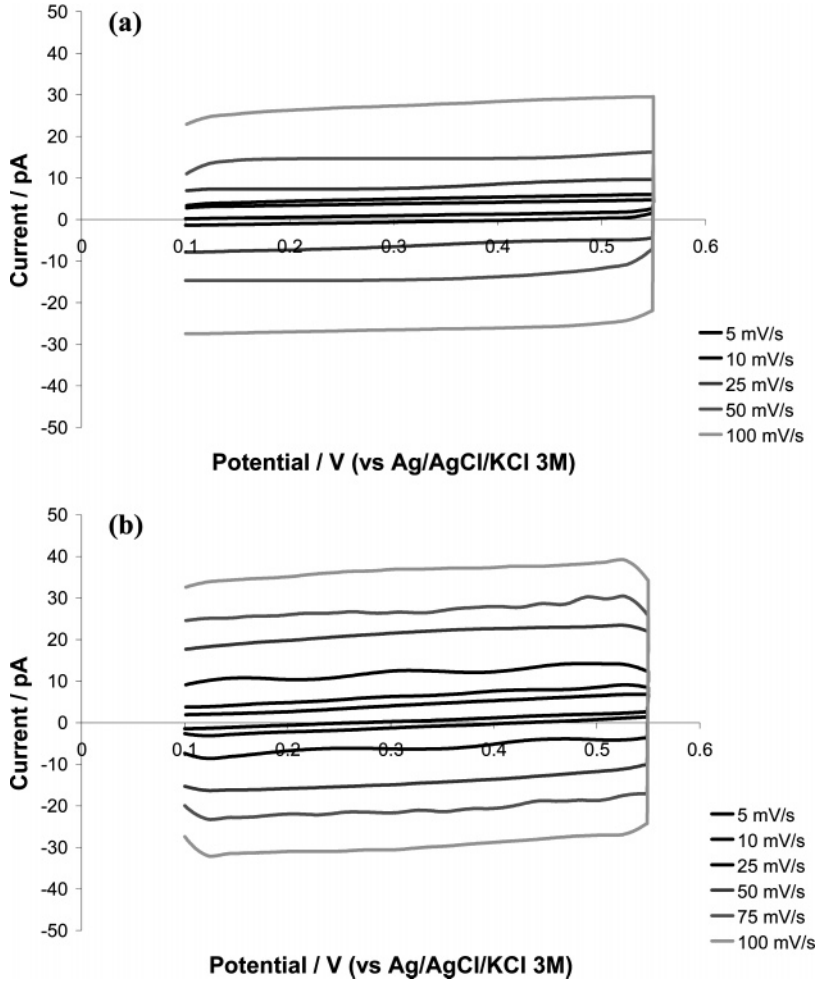

Figure 5. (a) Nanoelectrode response to electrolyte only (PBS, pH 7.4) at a 3 × 3 nanopore array with 80-nm pore radii; (b) the response of an unpatterned passivated electrode (with no nanopore openings) to 1 mM FcCOOH in PBS.

cone model (eq 3), for a typical set of experimental parameters, shows that the steady-state, diffusion-limited current at the cone-recessed disk is intermediate between that of the inlaid disk (eq 1) and the cylinder-recessed disk (eq 2). For example, taking the one-electron oxidation of FcCOOH in PBS solution as the test reaction, with the following parameters $n = 1$, $F = 96485$ C mol^{-1}, $C^b = 1 \times 10^{-6}$ mol cm^{-3}, $D = 5.3 \times 10^{-6}$ cm^2 s^{-1}, $L = 5 \times 10^{-5}$ cm (500 nm), $r_0 = 1.35 \times 10^{-5}$ cm (135 nm), and $r_L = 2.25 \times 10^{-5}$ cm (225 nm), the currents at inlaid, cylinder-recessed, and truncated cone-recessed disks are 27.6, 4.8, and 8.0 pA, respectively. This confirms the intuitive feeling for diffusion to an electrode recessed in a truncated cone: such diffusion is less hindered than to an electrode recessed in a cylinder but more hindered than to an inlaid disk electrode. A recent computational simulation study of such diffusion process confirms this suggestion.[39]

Table 1 summarizes data for the r_0 and r_L values extracted by application of eq 3 to the experimental data. It can be seen that r_0 values obtained from the truncated cone-recess model are ~7% smaller than the radii obtained by application of the cylinder-recess model (eq 2), suggesting that the cone shape of the recess has minimal influence on the diffusion-controlled current. Based on the data in Table 1, for $L = 500$ nm, $r_L = 225$ nm, and $r_0 = \sim 200$ nm, the wall angle is generally close to 3°, although ranging up to 7°, which satisfies one of the restrictions in the developed model ($\tan \alpha \ll 1$). These data are also in agreement with our assignment of wall angle values of ≤10° based on the SEM observations (Figure 2) as well as with the published[23,26] observations of FIB producing wall angles of 2−10°. All of these data are based on currents normalized for the number of pores in each array studied, so individual variation across an array are not accounted for. Overall, it can be summarized that the cone-recessed disk model (eq 3) is complementary to the SEM experimental observations and provides access to cone wall angles. The small values of the wall angles imply that the cylinder-recessed disk model (eq 2) may be used for qualitative description of these nanopore array electrodes. At the time scales used in this work, diffusion to the pore mouth is the controlling factor in the electrode behavior.

Capacitance. The capacitance of the electrodes was estimated from CV experiments using both nanopore array electrodes in PBS electrolyte solution without added FcCOOH and at buried electrodes, i.e., without milled nanopores, in the presence of FcCOOH in the PBS electrolyte solution (Figure 5). Under these

(34) Oldham, K. B. *Anal. Chem.* **1992**, *64*, 646−651.
(35) Baranski, A. S. *J. Electroanal. Chem.* **1991**, *307*, 287−292.
(36) Zhang, B.; Zhang, Y. H.; White, H. S. *Anal. Chem.* **2004**, *76*, 6229−6238.
(37) Zhang, B.; Zhang, Y. H.; White, H. S. *Anal. Chem.* **2006**, *78*, 477−483.
(38) Zhang, Y. H.; Zhang, B.; White, H. S. *J. Phys. Chem.* **2006**, *110*, 1768−1774.
(39) Britz, D.; Strutwolf, J. *Electrochim. Acta* **2006**, *52*, 33−41.

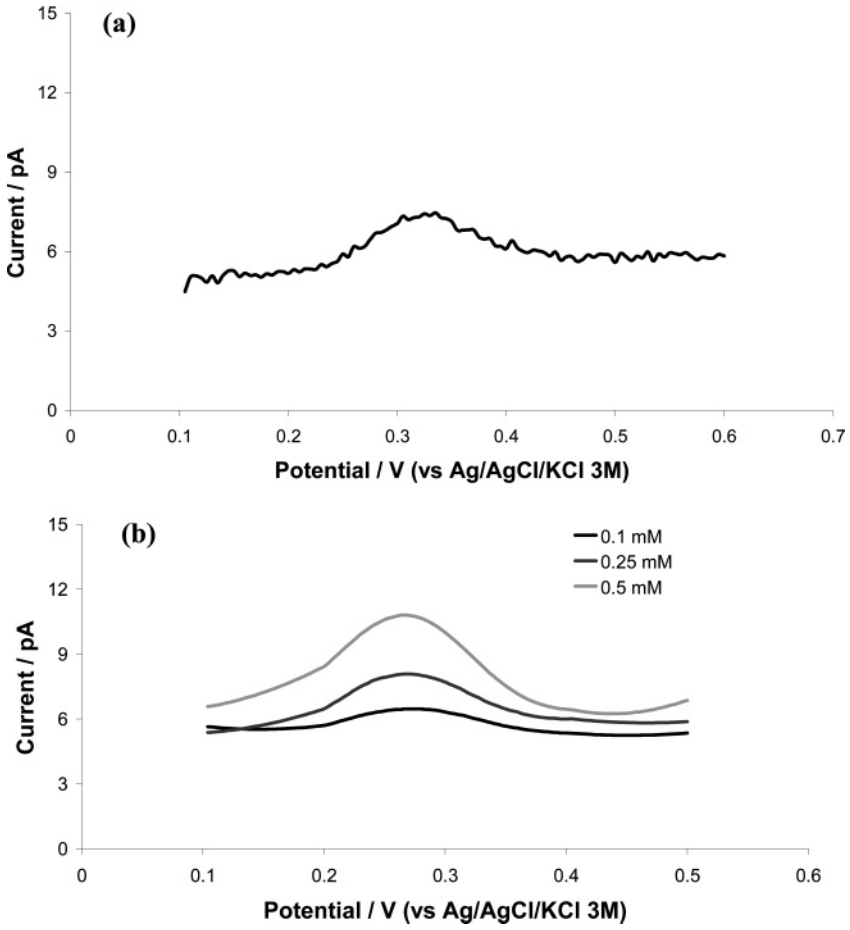

Figure 6. (a) Square wave voltammetry of 1 mM FcCOOH in PBS using a single nanopore electrode: $r_L = 225$ nm; $r_0 = 195$ nm (as calculated by application of eq 3). (b) Square wave voltammetry at different concentrations of FcCOOH in PBS at nanopore array electrode (5 × 5 array; $r_L = 100$ nm; $r_0 = 37$ nm).

circumstances, no faradic current was present. The capacitance values were determined from the charging currents measured at +0.4 V at a variety of sweep rates. In all cases, the capacitance was of the order of 0.02−0.03 μF cm^{-2}, regardless of whether nanopores were present or not; i.e., the presence of nanopores in the silicon nitride passivation layer did not change the capacitance of the structure. In this case, the capacitance is normalized to the geometric area of the patterned buried metal layer beneath the silicon nitride passivation layer and ignores any contributions from stray capacitances due to printed circuit boards, on-chip bondpads, and metal tracks.

Single Nanopore Electrode and Pulse Voltammetry Measurements. Voltammetry at single nanopore electrodes was achieved (Figure 3a inset), at which well-defined steady-state CVs were obtained. Application of pulse voltammetric techniques at these nanopore electrodes is also of benefit in defining future analytical possibilities. Figure 6 demonstrates square wave voltammetry at both a single nanopore electrode and at a nanopore array electrode. Application of such methods indicates that the capacitances of the electrode structures are sufficiently small to enable pulse voltammetric current sampling and thus will be of use in developing analytical applications of these devices.

CONCLUSIONS

The fabrication of nanopore array recessed disk electrodes was achieved by prototyping with focused ion beam milling. This technique is a direct-write method; small numbers of samples can be processed at a time (rather than whole wafers), and the pore dimensions, numbers, and interpore spacing can be easily controlled. The combination of these factors makes FIB milling a rapid and versatile technique for prototype nanoelectrode fabrication, with respect to more complex and lengthy procedures such as E-beam lithography. FIB milling has enormous practical relevance for the fabrication of prototypes and their subsequent experimental evaluation prior to use of more prolonged approaches to fabrication of engineered devices. The milling method creates a truncated cone-shaped pore, rather than a cylinder, and thus a model for diffusion-controlled current at a disk electrode at the base of such a truncated cone was developed. Application of this model to the experimental current data confirms that small cone wall angles were obtained, in agreement with SEM observations that this angle is ≤10°. The devices described here are amenable to electrochemical studies and offer opportunities for electroanalytical applications such as stripping voltammetry or nanobiosensor development. The fabrication of single nanopores as described and combination with electrochemical measurements provides a simple strategy for the study of ion detection methods based on nanopore transport. Use of pulse voltammetric methods will enable low-concentration measurements to be achieved. Further steps in the development of the electrochemistry of these devices is underway.

ACKNOWLEDGMENT

This work was supported by the European Commission (FP6-IST1-508774-IP "GOODFOOD: Food safety and quality with microsystems technology") and Science Foundation Ireland (02/IN.1/B84 (D.W.M.A.) and 02/IN.1/IM062 (J.P.G.)). The authors thank the Tyndall National Institute's Central Fabrication Facility for fabrication of the buried electrode devices and for access to the FIB system.

SUPPORTING INFORMATION AVAILABLE

Additional information as noted in text. This material is available free of charge via the Internet at http://pubs.acs.org.

Received for review October 6, 2006. Accepted February 5, 2007.

AC061878X